

Hydrogen-Bonded Organic Frameworks Based on Endless-Stacked Amides for Iodine Capture and Detection

Bin Li, Weiguang Qiu, Glenn P. A. Yap, Yves L. Dory,* and Jerome P. Claverie*

Recently, hydrogen-bonded organic frameworks (HOFs) have emerged as a rapidly advancing class of porous materials with significant potential for applications in the absorption and detection of various chemicals. Here, the unique ability of amide groups to form endless-stacking H-bonds is implemented in the design of HOFs. Starting from benzene-1,3,5-tricarboxamide and amide-containing tribenzocyclines as foundational building blocks, a diverse range of HOFs featuring 1D, 2D, or 3D hydrogen-bonded frameworks has been synthesized. Among those, all three porous HOFs, HOF_B-Hex, HOF_T-Pr and HOF_T-Hex exhibited permanent porosity, thereby demonstrating the effectiveness of amide-based HOFs strategy. Notably, HOF_T-Hex stands out with a 42% pore volume and an impressive iodine capture efficiency of 6.4 g g^{-1} . The iodine capture capacity is influenced not only by pore volume but also by the presence of accessible π -electrons within the material (i.e., electrons not engaged in a π - π stacking interaction). Furthermore, some of these HOFs exhibited fluorescent responses to iodine positioning them as highly promising materials for both the capture and sensing of iodine.

and ^{131}I), as the major volatile waste in nuclear fuel industry, posing substantial threats to both ecological environment and human health.^[2,3] The immediate capture and fast detection of radioactive iodine before its discharge has gained interest. Although silver-doped inorganic porous materials^[4] and organic amines-impregnated activated carbon^[5] have been utilized for radioiodine capture in the nuclear fuel industry, the development of new materials for iodine capture is still necessary due to their mediocre properties and notably low iodine capacity, high cost, and irreversible capture. Recently, a range of organic porous materials including porous organic polymers (POPs) and porous molecular crystals (PMCs) have been emerged as promising candidates for iodine capture due to their outstanding performance in this regard, notably high uptake capacity, repeatability, and rapid adsorption kinetics.^[6,7] POPs encompassing

conjugated microporous polymers (CMPs), polymers of intrinsic microporous (PIMs), hyper-cross-linked polymers (HCPs), covalent organic frameworks (COFs), and porous aromatic frameworks (PAFs) are connected by covalent bonds. In contrast, in PMCs, discrete organic molecules are connected by non-covalent interactions such as π - π interaction, hydrogen bond, and van der Waals interactions.^[8,9] Although POPs have proved to be highly effective iodine absorbents, elucidating the connection between their structure and iodine capture capabilities has proved to be challenging.^[6] This challenge arises from the fact that the majority of POPs exhibits amorphous or semicrystalline structures, providing a wide variety of chemical environments for iodine accommodation that are difficult to characterize. PMCs, in contrast, can be obtained as single crystals and their structure can be accurately characterized by single-crystal X-ray diffraction. Consequently, exploring the iodine capture performance of PMCs are paramount in unveiling the structure-activity relationship between the iodine bonding sites of organic adsorbents and iodine capture performance.

Within the plethora of organic porous materials reported as absorbents for iodine capture,^[6,10–23] it has been commonly observed that electron-rich heteroatoms and electron-donating groups such as $-\text{NH}-$,^[24,25] $-\text{N}=\text{C}-$,^[11,21,26,27] or alkynyl^[18,19,28,29] play an important role for iodine capture via the formation of charge-transfer complexes. However, the iodine uptake capacity of these materials varies significantly, even

1. Introduction

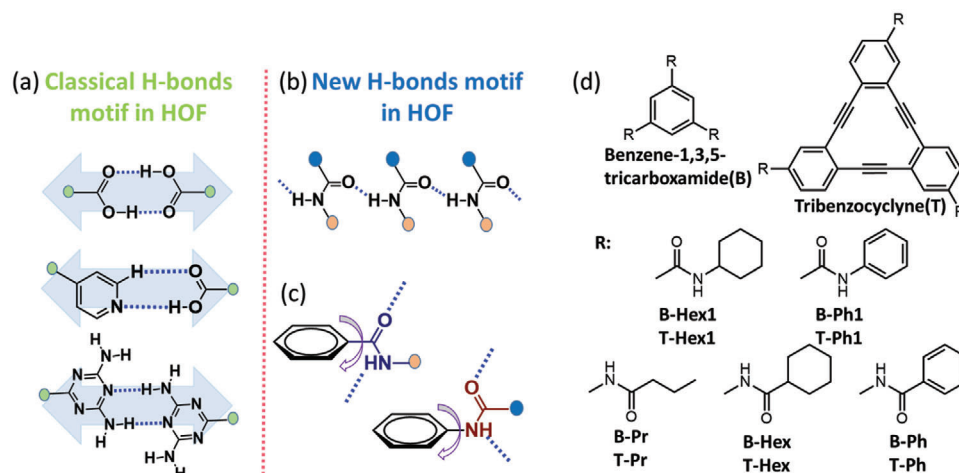
In the past decades, the nuclear industry has contributed to $\approx 10\%$ of the global electricity supply.^[1] Iodine radioisotopes (^{129}I

B. Li, W. Qiu, Y. L. Dory, J. P. Claverie
Department of Chemistry
Faculty of Sciences
Université de Sherbrooke
2500 Boul. de l'Université, Sherbrooke, QC J1K 2R1, Canada
E-mail: yves.dory@usherbrooke.ca; jerome.claverie@usherbrooke.ca
G. P. A. Yap
Department of Chemistry and Biochemistry
University of Delaware
Newark, DE 19716, USA
Y. L. Dory
Institut de Pharmacologie et Centre de Recherche du CHUS
Université de Sherbrooke
3001, 12e avenue nord, Sherbrooke, QC J1H 5N4, Canada

The ORCID identification number(s) for the author(s) of this article can be found under <https://doi.org/10.1002/adfm.202311964>

© 2023 The Authors. Advanced Functional Materials published by Wiley-VCH GmbH. This is an open access article under the terms of the Creative Commons Attribution-NonCommercial-NoDerivs License, which permits use and distribution in any medium, provided the original work is properly cited, the use is non-commercial and no modifications or adaptations are made.

DOI: 10.1002/adfm.202311964



Scheme 1. a) Terminal H-bonding motifs and their connectivity used for construction HOFs. b) Non-terminal H-bonding motif (amide) and its connectivity. c) Rotation of two types of amides relative to an aromatic core. d) Chemical structures of benzene-1,3,5-tricarboxamide (B) derivatives and tribenzocycline (T) derivatives.

when they have identical functional groups. For example, a series of porous polymers composed of phenyl and alkynyl group exhibit distinct iodine capture capacity between 0.97 and 2.15 g g^{-1} .^[14,18–20] These results indicate that the arrangement of the building blocks which controls pore size distribution is another crucial factor to take into account for iodine uptake capacity. Accordingly, several strategies, including expanding pore size/volume and increasing surface area, have been applied to construct organic absorbents with improved iodine uptake capacity.^[11,13,14,26] However, the relationship between these strategies and iodine uptake capacity remains ambiguous. For example, results from Kuang^[19] and Zhu^[18] have demonstrated that the iodine uptake capacity is not related to surface area of the materials, even though it is a common objective in the construction of porous absorbents. Nevertheless, Jiang^[11] concluded that pore volume is positively correlated with the uptake capacity based on a series of PB-DMTP COFs (TPB = triphenylbenzene; DMTP = dimethoxyterephthaldehyde).^[19] In addition, a new type of material named nonporous adaptive crystal^[30] also has been reported to be able to capture iodine despite being nonporous in its initial crystalline state. Therefore, further exploring the effects of material structure on iodine capture performance is still necessary.

In-depth understanding of how subtle differences in molecular structure affect the final crystal structure remains a fascinating facet of the supramolecular field.^[31,32] The self-assembly of specific building blocks via noncovalent interactions into various well-defined architectures such as 1D columns, 2D layered networks and 3D PMCs has been demonstrated in a myriad of examples.^[9,33–40] Among those, hydrogen-bonded organic frameworks (HOFs) have rapidly become an important class of well-defined PMCs connected by H-bond and which exhibit high crystallinity, recyclability and simple preparation conditions.^[38–45] However, the weaker nature of H-bond compared to covalent bonds remains a hurdle in the construction of HOFs with permanent porosity. As a result, most HOFs collapse after the removal of solvent. To address this issue, multiple H-bonds are often employed, as a higher number of H-bonds can result in stronger HOFs.^[39,45–51] Furthermore, the selection of hydrogen-bonding

motifs is a crucial factor in the construction of robust HOFs. Various hydrogen-bonding motifs, such as carboxylic acid, pyridine, pyrazole and imides have been employed in the construction of HOFs (Scheme 1a). Contrasting with the aforementioned functionalities, amides hold particular interest due to their ability to serve as both hydrogen-bond donors and acceptors, thus unlocking the possibility of endless-stacking where extended H-bonded superstructures are generated (Scheme 1b). Such characteristic is essential for directing protein folding and for the self-assembly of macrocycles into columns.^[33–35,52–55] Remarkably, the cooperative nature of amide group can lead to a significantly higher stabilization energy than the sum of individual contributions.^[53,54] For example, it is calculated that the H-bond between two formamide molecules accounts for a stabilization energy of 4.5 kcal·mol⁻¹. By contrast if a formamide molecule is engaged in an endless stacking scheme whereby a given amide group acts both as donor and acceptor, the stabilization is now 6.25 kcal·mol⁻¹ per H-bond. This cooperative effect should favor the construction of amide-based HOFs with robust structures and permanent porosity. To our knowledge, HOFs connected by amide-based H-bonding motifs have never been exploited. While an amide-based HOF (HOF-8) constructed by N¹, N³, N⁵-tris(pyridin-4-yl) benzene-1,3,5-tricarboxamide) was reported by Luo in 2013,^[56] the H-bond originated from an amide NH as donor and a pyridine as acceptor. Thus, the goal of this paper is to exploit the possibility of generating HOF materials based on endless stacking amides.

In this paper, two types of C₃ symmetrical molecules benzene-1,3,5-tricarboxamide (B) and tribenzocyclines (T) derivatives with different substituents were designed and synthesized (Scheme 1d). Unlike other hydrogen bonding motifs that remain coplanar with aromatic moieties, the H-bond formation in amides is so favorable that deviation from planarity is possible (Scheme 1a–c).^[57] Accordingly, the supramolecular arrangements in amide base HOFs are virtually endless. In this work, we have constructed 1D columns using T-Pr and B-Hex1, supramolecular sheets with B-Ph1, supramolecular porous crystals with T-Hex and B-Hex and dense structures with B-Pr, B-Ph,

and T-Ph. Starting from these diversified structures, we demonstrate that not only pore volume, but also accessible π -electrons in the material (i.e., electrons not engaged in a π – π stacking interaction) are the essential factors affecting the iodine capture capacity. Among these supramolecular crystals, T-Hex which exhibits high porosity and abundant free π -electrons, shows excellent iodine capture performance including high uptake capacity in both vapor and aqueous solution (6.4 and 3.6 g·g⁻¹, respectively) and fast adsorption kinetics. Meanwhile, T-Pr is a promising iodine sensor as it displayed rapid fluorescence response and sensitivity to iodine. Our research not only expands the pathways for constructing novel HOFs materials, but it also deepens the understanding of the iodine capture mechanism with organic materials, providing valuable insights for the development of novel adsorbents for iodine capture.

2. Results and Discussion

2.1. Molecular Design and Synthesis

The beauty of using amides in the construction of self-assembled structures lies in the fact that the amide groups can be located anywhere within the skeleton of the molecule, while other H-bond forming groups such as carboxylic acid, pyridine, pyrazole, and imide^[39,40] are terminal groups (Scheme 1a). Consequently, for the latter situation, the H-bond is aligned with the two extremities of the molecules it connects. Such arrangement leads to the linear extension of the structure (Scheme 1a). By contrast, with amides, H-bond can conceptually be used to connect to molecules in the same plane but at an angle^[58] or even in a non-coplanar arrangement, greatly increasing the numbers of structures that are accessible^[33,35,59–65] (Scheme 1c). In this study, we explored two basic tectons with D_{3h} symmetry: benzene-1,3,5-tricarboxamide (B) and tribenzocyclyne (T). Since the steric effect of substituent is expected to play an important role in the directionality of the amide H-bond relative to an aromatic core, we explored three types of substituents, n-propyl, cyclohexyl and phenyl substituents, either attached to the N or C terminus of the amide, resulting in 10 supramolecular units (Scheme 1d). The B units were synthesized^[66] following the route depicted in Schemes S3 and S4 (Supporting Information) while the T units were synthesized (Schemes S1 and S2, Supporting Information) by cyclotrimerization reactions of the corresponding precursors compound 8, 9, 10, 18, 19 via a Stephens-Castro-type reaction.^[67,68]

2.2. Crystal Structure

Single crystals suitable for X-ray diffraction were obtained by vapor diffusion of hexane into tetrahydrofuran (THF) solution for T-Pr, B-Hex1, T-Ph, T-Hex, and vapor diffusion of CH₂Cl₂ into THF for B-Hex, and by slow evaporation of dimethyl sulfoxide (DMSO) solution for B-Ph1 and B-Pr. We were unable to crystallize T-Hex1 and T-Ph1, and crystal structure of B-Pr1 has already been reported.^[69] Note that T-Hex1 and T-Ph1 did not exhibit significant iodine uptake, so the lack of crystallographic information was not found to be problematic. Diffraction parameters

and crystal data for all other molecules are presented in Tables S1–S3 (Supporting Information). In view of the patterns for H-bond connectivity, these crystals can be roughly divided into four types:

- i. **1D H-bond chains** for T-Pr and B-Hex1. B-Hex1 crystallized in a monoclinic crystal system and $P-2_1/n$ space group. In the crystal (Figure 1a,d), each molecule is connected via H-bonds to another two units, respectively above and below, the unit under consideration, leading to a columnar stacking with the phenyl planes orthogonal to the column axis at a 0.34 nm interplanar distance. Although the placement of phenyl rings directly above each other is known to be unfavorable, the energetical cost is here overcome by the fact that all three amides in the molecule are engaged in continuous 1D H-bond chains. By contrast, T-Pr crystallizes in a monoclinic crystal system and $C-2/c$ space group. In the crystal, there are only two amides of T-Pr (Figure 2) involved in the H-bond while the remaining one is free. Within each column, the two lines of continuous 1D H-bond chains force the T cores to stack in a parallel fashion along the c axis but at a 45.77° tilt angle. Meanwhile, 1D channels are generated in between the columns (Figure 2) owing to the triangular geometry of the T-Pr molecule (pore volume: 2.2%).
- ii. **2D H-bond network** for B-Ph1. B-Ph1 was co-crystallized with DMSO in the past,^[70] showing H-bonds between DMSO and the B-Ph1 amides. We prepared solvent-free crystals which exhibit a different packing motif. In our case, B-Ph1 crystallized in a monoclinic crystal system and $P-2_1/n$ space group. There are two different conformations present in the crystal, referred to as M1 (yellow) and M2 (brown) (Figure S1a,b, Supporting Information). These conformations differ by their dihedral angles between the amide group and aromatic core. As shown in Figure S1c (Supporting Information), each M1 unit is connected two other M1 units by one H-bond each and connected to two M2 units by two H-bonds each. Further extension of the H-bond pattern along with a- and c-axis results in a 2D H-bond network, consequently leading to the formation of a supramolecular sheet architecture (Figure 1b,e).
- iii. **Lamellar 3D H-bond network** for T-Ph. T-Ph crystallized in a trigonal crystal system and R3 space group and each molecule possesses C₃ symmetry. In the crystal, each molecule is connected to six others, which makes the H-bonds extend in three dimensions, resulting in a 3D H-bond network (Figure 1c,f). This 3D H-bond network leads to a layered dense packing. The distance between two layers is 3.4 Å. Due to the almost planar conformation and triangular geometry of T-Ph, a cavity with 0.85 nm in diameter was generated by three adjacent co-planar molecules (Figure S2, Supporting Information) which are filled with H₂O residual solvent. Remarkably, there is no H-bond generated between amides and water molecules indicating the high stability of the 3D H-bond network. A lamellar 3D H-bond network is also observed with B-Ph and with B-Pr as shown in Figure S3 (Supporting Information).
- iv. **Non-layered 3D H-bond network** for B-Hex and T-Hex. B-Hex crystallizes in a cubic crystal system and $P23$ space group. In the crystal of B-Hex, two conformations exist,

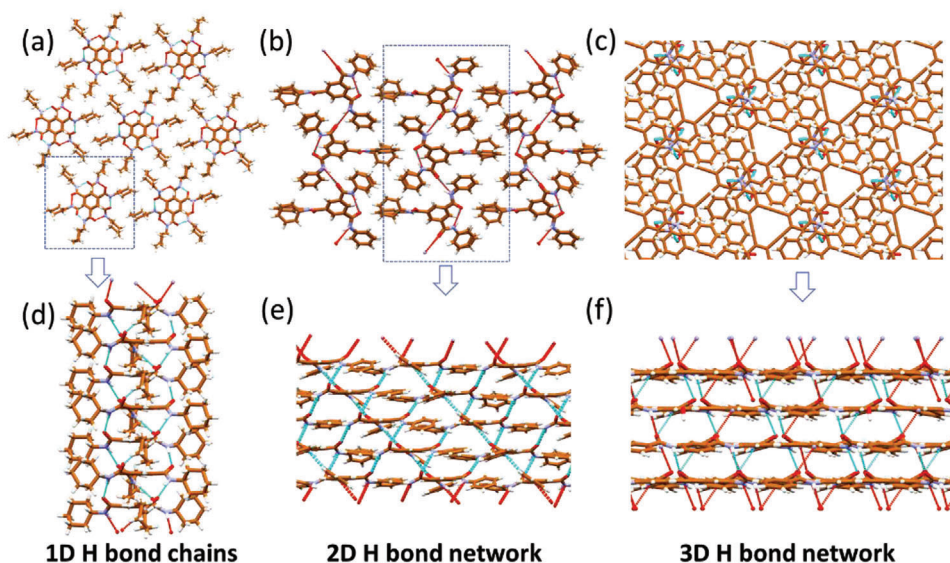


Figure 1. Representation of three types of H-bond connectivity (1D H-bond chains, 2D H-bond network, and 3D H-bond network) and corresponding to crystal structures in top view a–c) and side view d–f) of B-Hex1, B-Ph1 and T-Ph, respectively. H-bonds are shown as blue dotted lines.

referred as M1 (brown) which is non-symmetric, and M2 (yellow) which is C_3 symmetric (Figure 3a). As shown in Figure 3b, each M2 molecule is connected to three M1 partners by two H-bonds each from two separate amides for a total of 6 H-bonds per M2 unit. If this C_3 symmetric unit containing 4 molecules (one M2 and three M1) is defined as a building block (Figure 3c), one-unit cell is formed by stacking four building blocks via the remaining H-bond between M1 molecule (Figure 3d). Their assembly (Figure 3e) leads to the formation of large pores (0.5 and 1 nm in diameter) between unit cells. These pores are interconnected and extend into 3D (Figure 3f) with pore volume is 11.5%.

T-Hex crystallizes in a R_3 space group. In terms of symmetric equivalence, four conformations exist in the crystal referred to as M1 (light blue), M2 (dark blue), M3 (yellow), and M4 (brown), respectively (Figure 4a). M1 and M2 are C_3 symmetric and the connectivity of these two types of molecules are same: each M1 and M2 molecule is connected to six M3 and M4 molecules respectively (Figure S3, Supporting Information). As shown in Figure 4b,c, six M4 molecules are connected by an H-bond cycle with six amides utilizing 6 H-bonds. M3 has the same connectivity (Figure 4d). If a building block (Figure 4c) is defined by these six M3 or M4 molecules, each building block is connected to six others by two H-bonds from two amides respectively (Figure 4d), their assembly leads to a porous crystal (Figure 4e) constituted of channels of ≈ 1.5 nm in diameter extending either in the a or c direction. The pore volume of T-Hex is high with a calculated value of 42.4% (Figure 4f). It should be clarified that the crystallographic pore volume corresponds to the space within the crystal that can accommodate a sphere of an arbitrarily-chosen radius, here set at a value of 1.4 \AA .^[80]

As shown above, the use of amide groups results in a wide diversity for the packing of core building blocks. Nonetheless, their assembly is governed by several directing concepts. 1) **Side chain effect:** For molecules with cyclohexyl as side chains (B-Hex1, B-Hex, and T-Hex), the cyclohexyl group tends to be orthogonal to the aromatic core owing to its steric effect, thus leading to helical column stacking or porous stacking. In contrast, molecules with phenyl groups as side chains (B-Ph1, B-Ph, and T-Ph) adopt an almost coplanar conformation resulting from a decreased steric hindrance and from conjugation effects. Such arrangement leads to layered stacking as shown in Figure 1. A slightly out-of-plane phenyl group observed in B-Ph and T-Ph1 is attributed to the competition between conjugation which favors planarity and intermolecular H-bonds which forces the amide in an out-of-plane conformation. 2) **Amide group connectivity:** The different connections between the amide group to the T/B cores (T/B-CONH or T/B-NHCO) also determine distinct crystal

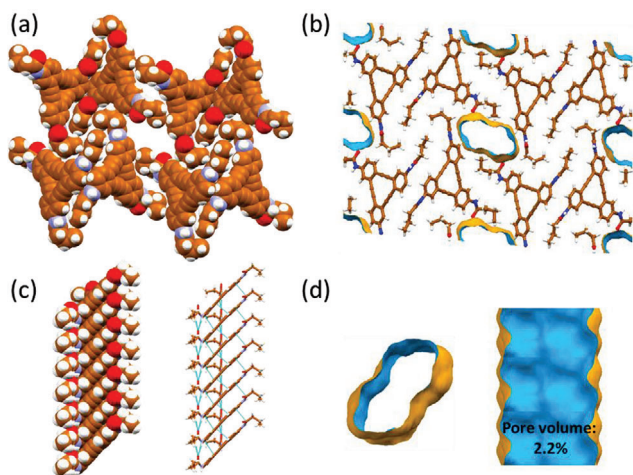


Figure 2. Crystal structure of T-PR. Packing diagram in a) top view and c) side view. b) The visualized surface of 1D surface in the crystal and d) cross-section of one channel. The outside color is yellow, and the inside color is blue. The channels are filled with THF molecules, which are not shown due to disorder. H-bonds are shown as blue dotted lines.

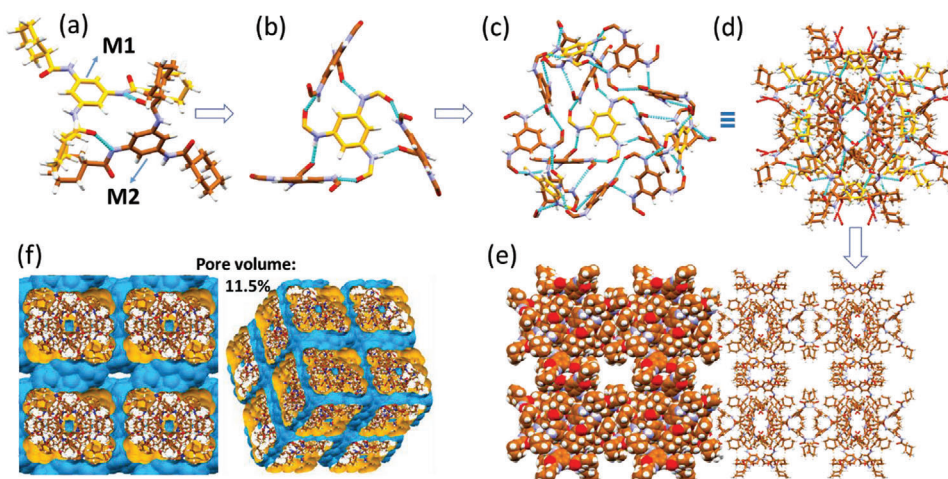


Figure 3. Crystal structure of B-Hex. a) Molecular conformations of B-Hex in the crystal. b) diagram of individual molecules connected to others via H-bond. c,d) Molecular packing in one crystal unit cell with intermolecular H-bond. (c) Without and (d) with the cyclohexyl group. e) Stacking along the b axis. f) Solvent-accessible surface (in blue) showing 3D horizontal and vertical connected channels in the crystal with respective pore sizes of 1.5 and 0.5 nm (the bulk is shown in yellow). In (b,c), the cyclohexyl ring is omitted to for the sake of clarity. H-bonds are shown as blue dotted lines.

structures which is confirmed by the crystal structures of B-Ph and B-Ph1, as well as B-Hex and B-Hex1 (Table S4, Supporting Information). The conformation of above-mentioned molecules in the crystal is consistent with the optimized conformation of three model molecules (Figures S5–S7, Supporting Information) with minimum energy which were obtained via Ramachandran plot. 3) **Core effect:** Notably, even though B-Ph and T-Ph both crystallize in the same space group with same connectivity, a cavity is only generated with T-Ph. This cavity is large enough to accommodate water molecules. In fact, large cavities are only obtained with the T building block. Although changing the shape of the building block drastically alters its packing characteristic, the size of

the voids in the packed structure scales with the critical dimension of the building block.^[71] Thus, significant solvent/analyte accessibility will only be achieved with T as building block.

2.3. Porosity and Stability of the Crystals

As with most of the organic porous crystals, the pores of the generated crystals by T-PR, B-Hex, and T-Hex are filled with solvent molecules that support the framework of the porous crystals. To distinguish between molecules and their self-assembled porous crystals, we have named the resulting HOFs as follows:

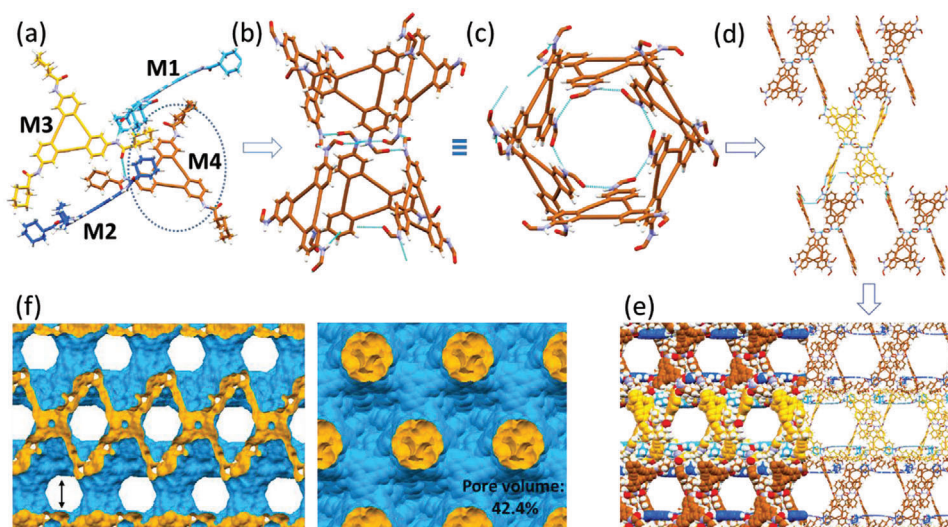


Figure 4. Crystal structure of T-Hex. a) T-Hex conformation in crystal. b) Diagram of connectivity of M4 molecules (brown) via H-bond and their further stacking c) in top view and d) side view showing also M3 units (yellow). e) Stacking diagram along a axis for all four units (M1 clear blue, M2 dark blue, M3 yellow, and M4 brown). f) Accessible surface (solvent accessible: yellow, bulk: blue) showing 2D connected channels. For the sake of clarity, cyclohexyl is omitted in (b–d) to clarify the view. H-bonds are shown as blue dotted lines. The interconnected channels are filled with solvents, which are omitted due to disorder.

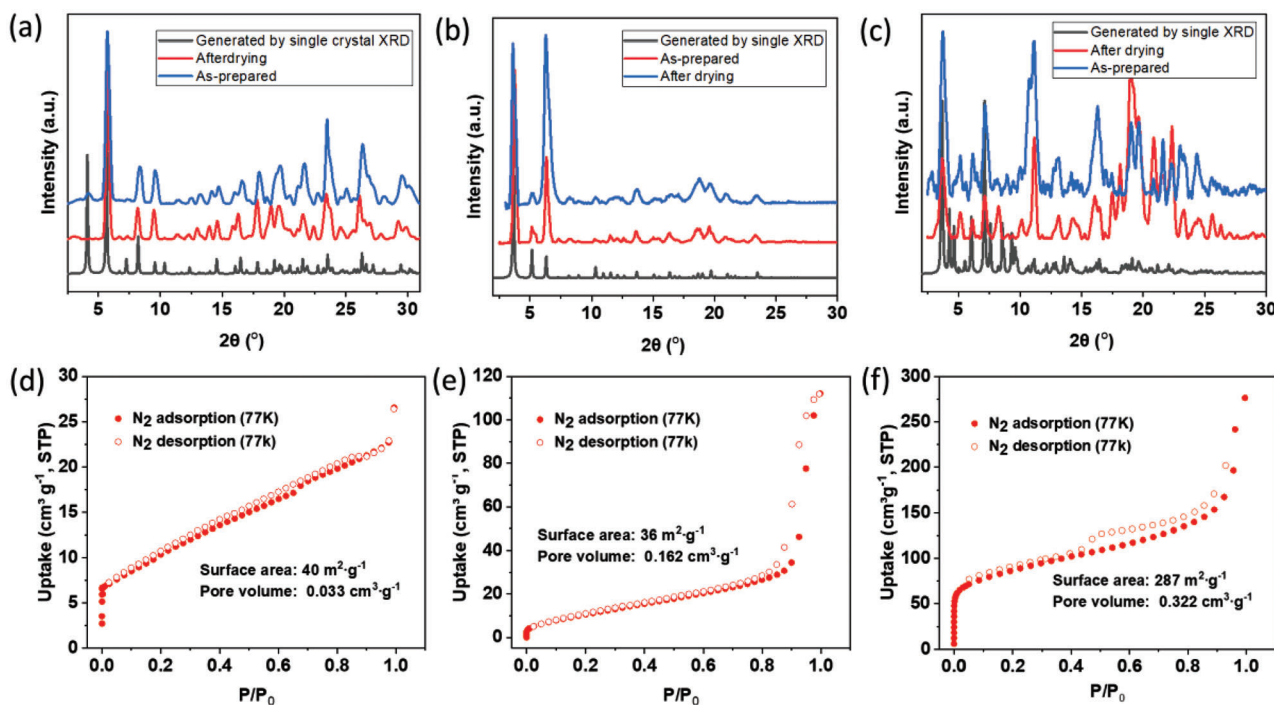


Figure 5. PXRD patterns of a) HOF_T-Hex, b) HOF_T-Pr, and c) HOF_B-Hex. Nitrogen adsorption (solid symbols) and desorption (hollow symbols) curves at 77 K of d) HOF_T-Pr, e) HOF_T-Pr, and f) HOF_T-Hex.

HOF_T-Pr, HOF_B-Hex, and HOF_T-Hex, corresponding to their respective molecular names. Due to the fragile nature of H-bonds, mild conditions should be used to remove these solvent molecules in order to preserve the inherent porosity of the structure. In our case, the fresh crystals were immersed in hexane for 24 h, followed by air-drying for two weeks. As shown in Figures S8–S10 (Supporting Information), a plateau is maintained until 350 °C in all thermogravimetric (TGA) curves, indicating that the dried crystals remain thermally stable below this temperature. In addition, there is no weight loss observed before this decomposition temperature indicating that all solvents have been removed upon drying. Powder X-ray diffraction (PXRD) was also performed to investigate the crystallinity before and after drying. As shown in Figure 5a–c, the PXRD patterns of the dried and solvated powders are very similar, thus suggesting retention of the main structural characteristics (see Figures S11–S13, Supporting Information, for indexed diffractograms). Differences in peak heights are unavoidable and originate from changes in electronic density between solvent-filled and empty samples. Thus, the arrangement of the molecules within the crystal is retained upon drying. This advantageous structural stability is expected as amide groups are connected to each other via H-bonds without binding to solvent molecules. The permanent porosity of these three porous crystals was evaluated by N₂ (Figure 5d–f) and CO₂ gas sorption experiment (Figures S17–S19, Supporting Information). For example, T-Hex has a type IV isotherm (Figure 5f) with calculated BET (Brunauer-Emmett-Teller) surface of 287 m²·g⁻¹ (N₂ probe) or 457 m²·g⁻¹ (CO₂ probe) (see Table S5, Supporting Information). The average pore size is ≈ 3 nm (as analyzed by DFT analysis, Figure S14, Supporting Information). Note that this average distance is slightly larger than the measured distance

in Figure 4f because the latter corresponds to the shortest distance between two opposite sides of the pore. These BET results confirm the permanent porosity of T-Hex, B-Hex, and T-Pr. The values of BET surfaces and pore volumes are commensurate with reported literature HOFs (Table S6, Supporting Information).

2.4. Iodine Capture in Vapor and Aqueous Solution

The iodine capture performance of all emptied (dried) crystals were evaluated by gravimetric measurements method. As shown in Figure 6d, HOF_B-Hex, HOF_T-Pr and HOF_T-Hex show significant iodine capture capacity of 0.92, 1.5, and 6.4 g g⁻¹, respectively, accompanied by a remarkable color change (Figure 6a,b), while the other crystals could only capture < 0.1 g g⁻¹. All the crystals reached absorption equilibrium within 3 h. The iodine capture capacity of HOF_B-Hex, HOF_T-Pr, and HOF_T-Hex measured by gravimetry is similar to the one measured by TGA results (Figures S8–S10, Supporting Information) which showed mass losses of 48%, 52%, and 86.5%, respectively, before their corresponding decomposition temperature. In addition, the sorption kinetics for iodine capture of HOF_T-Hex was simulated with a pseudo first-order kinetic model and a pseudo second-order kinetic model (Figures S20 and S21, Supporting Information). The results better matched with the pseudo second-order kinetic model, indicating the absorption process is dominated by chemisorption.^[72] The K_{80%}, which represents 80% of the full adsorption capacity, is an important indicator for evaluating the iodine capture performance, as adsorbents are usually replaced before reaching 80% of their full capacity.^[26,73] The calculated K_{80%} of HOF_T-Hex is 2.8gh⁻¹ which is higher than most of the

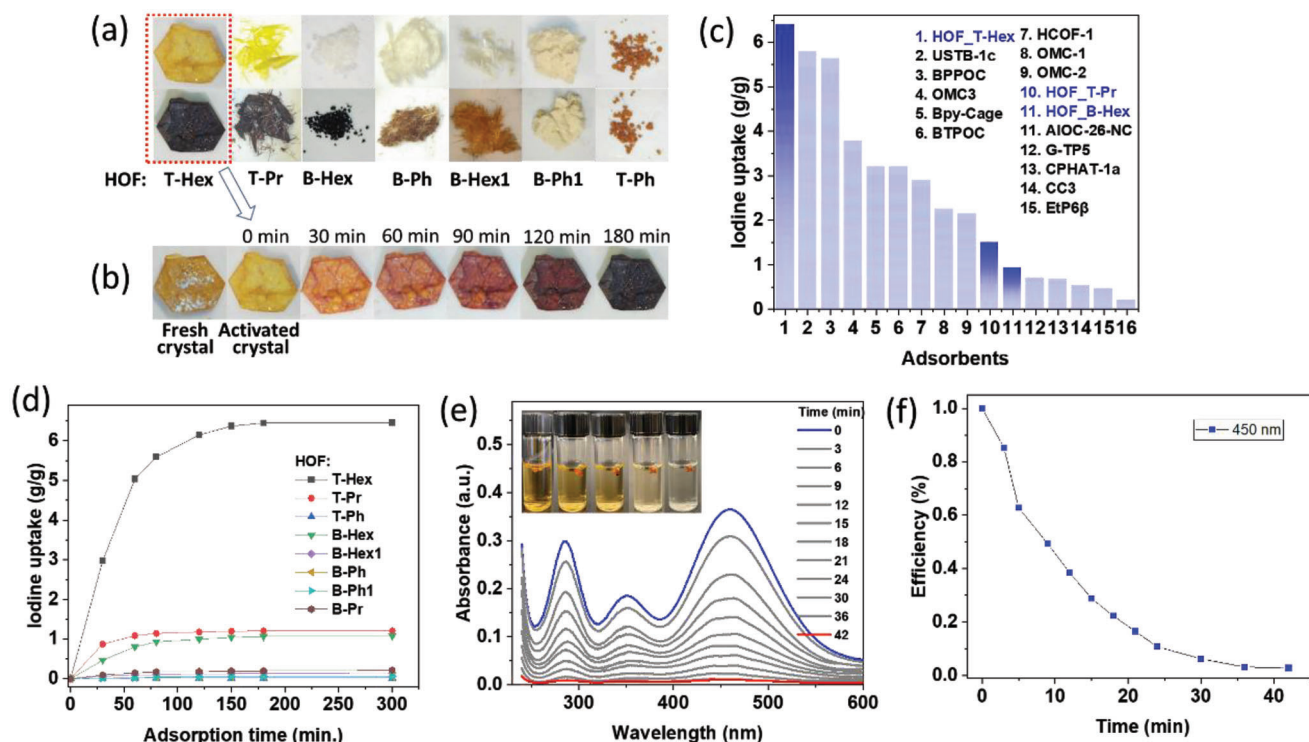


Figure 6. a) Photography of constructed supramolecular crystals before (top) and after (bottom) iodine capture. b) Photography of HOF_T-Hex single crystal at different time intervals during iodine capture process (crystal diameter is 0.5 cm). c) Iodine capture capacities of different adsorbents. d) Gravimetric measurement of iodine capture capacities of supramolecular crystals as function of time at 75 °C. e) Time dependent UV/vis spectra of iodine aqueous solutions upon addition of HOF_T-Hex crystal. Insert: photos of saturated iodine aqueous solution after addition of HOF_T-Hex crystal. f) calculated iodine capture efficiencies at various times.

reported adsorbents.^[26,73] It is worth mentioning that HOF_T-Hex has the highest iodine capture value among all the reported PMCs including porous organic cage, non-porous adaptive crystal and HOFs (Figure 6c). Furthermore, even when compared with all reported iodine adsorbents, HOF_T-Hex exhibits a high iodine capture capacity, ranking in the top 7 of all reported materials for iodine capture (Table S7, Supporting Information).

Based on the excellent iodine vapor capture performance of HOF_T-Hex, its iodine capture performance was also evaluated in aqueous solution. Upon addition of HOF_T-Hex (5 mg) to a saturated iodine aqueous solution (1.2 mM; 2.5 mL), the iodine concentration decreases over time (Figure 6e,f) to virtually zero in 35 min, with a final concentration of iodine in aqueous solution of < 5 ppm which was determined by the UV-vis absorption intensity of iodine (Figures S22 and S23, Supporting Information). The iodine capture capacity of HOF_T-Hex in aqueous solution was found to be 3.2 g·g⁻¹. To the best of our knowledge, this iodine capture capacity value of HOF_T-Hex in aqueous solution is superior to that of reported materials, except for a single ionic porous polymer.^[74]

2.5. Adsorption Mechanism

Given its high iodine capture capacity, HOF_T-Hex was chosen to study the iodine capture mechanism, which was completed by Raman spectroscopy (RM), X-ray photoelectron spec-

troscopy (XPS), ¹H nuclear magnetic resonance (NMR) and powder X-ray diffraction (PXRD). RM was first used to identify the iodine species trapped in HOF_T-Hex (HOF_T-Hex iodine). As shown in Figure 7b, HOF_T-Hex_iodine presents two bands at 110 and 160 cm⁻¹, associated with the symmetric stretching vibration of polyiodide anions I₃⁻ and I₅⁻ respectively.^[75] The presence of polyiodide anions was also confirmed by XPS. Two broad peaks were observed in I_{3d} XPS spectrum which could be resolved into two peaks which correspond to I₃⁻ (618.3 and 629.7) and I₅⁻ (620.49 and 631.9), respectively (Figure 7a).^[76,77] These generated polyiodide anions can be explained by the presence of a charge transfer between the electron-rich T-Hex framework and the captured iodine, as also observed in previously studied organic porous adsorbents.^[13,15,16,73] To evaluate the bonding sites of iodine to T-Hex, ¹H NMR titration experiments of T-Hex with iodine were performed in THF using a 7.05T magnet (Figure 7d), which were then used to determine the association constant K_a between T-Hex and iodine (Figure 7d). As the mole ratio of T-Hex to iodine increases from 0.5 to 4, the benzene ring proton resonance gradually shifts, while the peripheral cyclohexyl protons resonances remain almost unchanged. The Raman bands of the triple bonds (2212 cm⁻¹) in HOF_T-Hex also did not shift upon absorption of iodine (Figure S24, Supporting Information). This suggests that iodine is bound to the benzene rings of HOF_T-Hex through the formation of charge transfer complexes. In addition, the ¹H NMR titration experiments with B-Hex and -Pr (Figures S25 and S26, Supporting Information) in THF suggest a similar

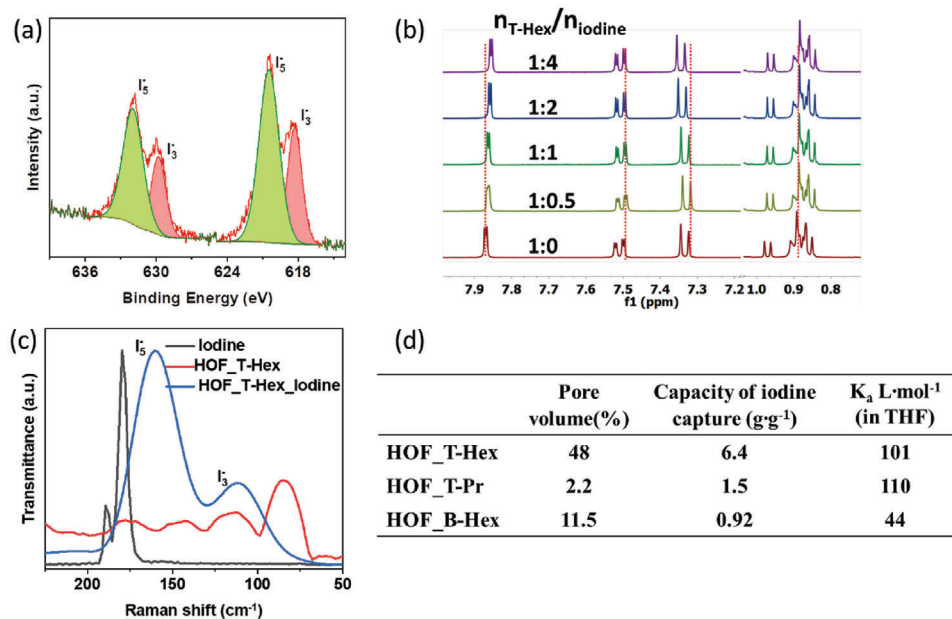


Figure 7. a) XPS spectra of HOF_T-Hex after iodine capture. b) ¹H NMR spectra of T-Hex (1 mg mL⁻¹ in THF) upon addition of iodine. c) Selected Raman spectra of HOF_T-Hex before and after iodine capture. d) Pore volume, iodine capture capacity and association constant to iodine (in THF) for HOF_T-Hex, HOF_B-Hex, and HOF_T-Pr.

mechanism, indicating the formation of a charge transfer complex between the benzene rings and the polyiodide. No diffraction peaks were observed for HOF_T-Hex_iodine (Figure S29, Supporting Information). This may indicate that the HOF structure is disorganized upon inclusion of the large amount of iodine that is included within the structure. It is also conceivable that the HOF structure is conserved, but, in the XRD analysis, the scattering by the disordered iodine molecules hides the less intense diffraction pattern of the HOF. Unfortunately, iodine is so tightly bound to T-Hex that it was not possible to remove it entirely from the T-Hex_iodine. Thus, we could not assess whether the structure was recovered upon iodine removal. It should also be mentioned that iodine may not only be trapped within the HOF, but also adsorbed at its surface.

Based on an analysis of both iodine capture capacity and crystal structure of all the prepared molecules, it can be concluded that the presence of pore volume is required to capture iodine. For example, crystal of T-Ph, which contains a high number of phenyl groups, has virtually zero iodine capture capacity, as expected from its absence of porosity. However, there is no simple correlation between pore volume and iodine capacity (Table S8, Supporting Information). For example, HOF_B-Hex has a higher pore volume but a lower iodine capacity than HOF_T-Pr. The pores in HOF_T-Pr are decorated with phenyl groups whereas all phenyl groups in HOF_B-Hex are buried inside the walls of the HOF network. Thus, HOF_T-Pr has a larger iodine association constant K_a in solution (Figure 7d) than HOF_B-Hex and a larger iodine capture, which is consistent with the fact that iodine preferentially binds to aromatic groups. Following this argument, HOF_T-Hex, which offers both a high pore volume and a high number of accessible phenyl groups has the highest iodine capacity of all HOFs tested here (Table S8, Supporting Information).

2.6. Iodine Detection

Rapid detection of iodine vapor is essential for advance warning and assessment of contamination. In combination with its excellent iodine capture performance, crystals based on T were evaluated for their ability to act as iodine sensor. For practical usage, a fluorescent film of HOF_T-Pr was prepared on a quartz plate (see SI). This ability to easily form a film from a concentrated THF solution was ascribed to the presence of flexible propyl groups that endows solubility even at high concentration. As shown in **Figure 8**, when the test film was placed in a bottle filled with iodine vapor at 25 °C, its fluorescent intensity dropped sharply to 16% of the initial value within 1 min (Figure 8b). This fluorescence quenching is associated to the formation of a charge transfer complex between HOF_T-Pr and iodine. As the exposure time increased, fluorescent quenching further increased, eventually reaching 99.8% in 5 min (Figure 8c). This fluorescent quenching process was easily monitored by naked eyes under visible light or UV. As shown in Figure 8a, the fresh light-yellow film turned gradually brown as exposure time increased. In comparison, the color change of the film was more pronounced under light at 365 nm UV (from bright yellow to black). To quantify the quenching efficiency of iodine to T-Pr, an iodine titration experiment was performed in THF solution. As shown in Figure 8d, the fluorescent intensity of T-Pr gradually decreased in the presence of 30 equivalents of iodine in THF. Remarkably, once the fluorescent intensity was quenched, it could be recovered by simply stopping the exposition of the HOF_T-Pr film to iodine vapors (Figure 8e). The kinetics of fluorescence recovery was rapid (< 5 min), and the sensor could be repeatedly reused. Furthermore, we assessed the sensing capabilities of the T-Pr film at varying temperatures. As illustrated in Figure 8f, the film showed pronounced quenching efficiency over diverse temperature ranges. The detection limit

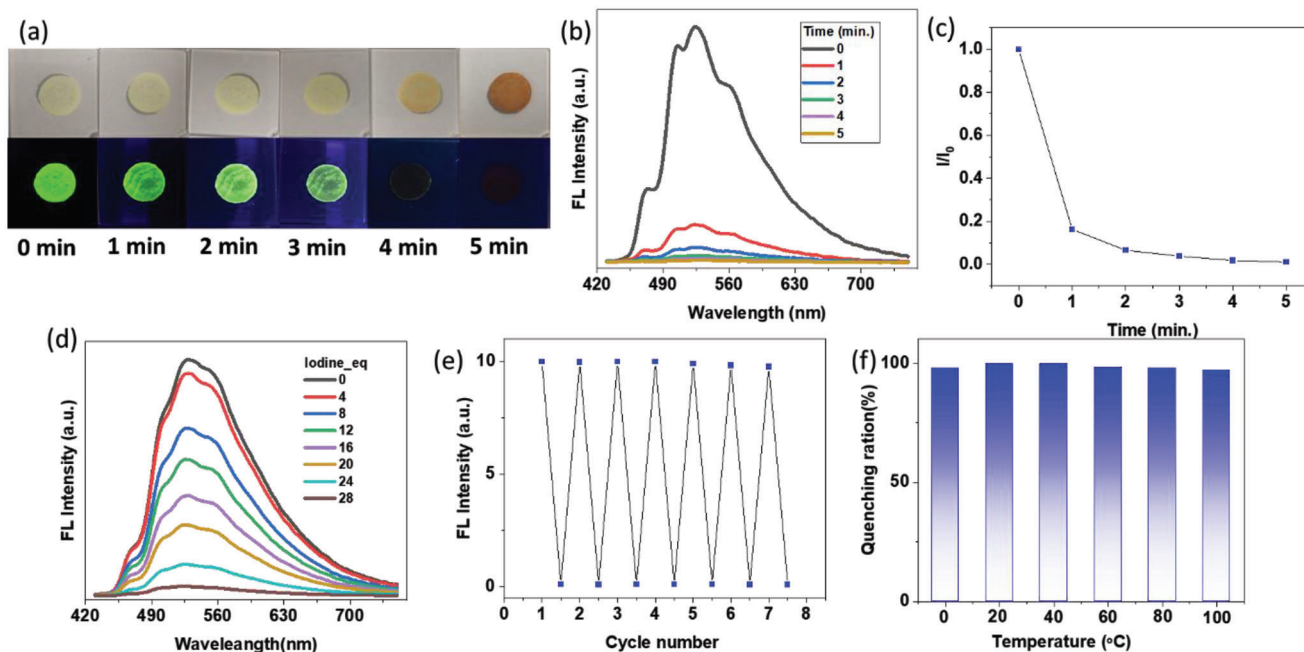


Figure 8. a) Photography under visible light (top) and 365 nm UV light (bottom) and b) fluorescent emission spectra c) fluorescent quenching efficient of HOF_T-Pr film upon exposure to iodine vapors at room temperature. d) Emission spectrum of T-Hex with different equation of iodine in THF. e) Reusability of HOF_T-Pr film as a sensor for iodine vapor sensing f) Quenching efficiency of fluorescent HOF_T-Pr film at different temperature under 100% humidity.

of T-Pr film was found to be $7.45 \times 10^{-7} \text{ mol} \cdot \text{L}^{-1}$ (Figure S30, Supporting Information), surpassing some of the inorganic or gel sensors for detecting iodine vapors.^[78,79] Given its rapid and sensitive iodine detection capability, the HOF_T-Pr film emerges as a potentially promising sensor for real-time iodine detection.

3. Conclusion

In conclusion, the endless stacking H-bonding mode of amides has been explored here for the preparation of a variety of HOFs. Unlike other H-bonding modes that are essentially unidirectional, the endless stacking H-bonding mode allows to connect units through a variety of spatial arrangements such as 1D H-bonding chains, 2D H-bonding networks, lamellar 3D and non-layered 3D networks, all of which were encountered in this work. Starting from two building blocks, T and B, a unique set of diverse supramolecular architectures was thus unraveled, demonstrating the great versatility of the endless-stacking H-bonding mode. As these materials are analogous in terms of chemical structure (but not of architecture), it thus became possible to clearly delineate the relationships between iodine capture capacity and supramolecular architecture. Although the presence of a pore volume is necessary to capture iodine, the presence of accessible p-electrons also plays a role. Based on such assessment, HOF_T-Hex, which has a 42% permanent pore volume with a high number of accessible phenyl groups, offers the highest iodine capture capacity so far reported for HOFs. By contrast, HOF_T-Pr has a lower pore volume and accessible phenyl groups but very flexible side groups which allowed the facile preparation of a sensor film which was found to be efficient for the detection of iodine vapors. Thus, this study demonstrates the unique ver-

satility of endless-stacked amide groups for the construction of HOFs.

Supporting Information

Supporting Information is available from the Wiley Online Library or from the author.

Acknowledgements

This research was supported by grants from les Fonds de Recherche du Québec, Nature et Technologie (FQRNT), the Canada Research Chair program, the Canada Foundation for Innovation, and the Natural Sciences and Engineering Research Council of Canada

Conflict of Interest

The authors declare no conflict of interest.

Data Availability Statement

The data that support the findings of this study are openly available in Zenodo <https://zenodo.org/records/8377966> or using the DOI: 10.5281/zenodo.8377966.

Keywords

amide, hydrogen bonding organic framework, hydrogen bonds, iodine capture, porous stacking

Received: September 28, 2023

Revised: November 10, 2023

Published online:

- [1] Y. Xie, T. Pan, Q. Lei, C. Chen, X. Dong, Y. Yuan, W. A. Maksoud, L. Zhao, L. Cavallo, I. Pinnau, Y. Han, *Nat. Commun.* **2022**, *13*, 2878.
- [2] G. Mushkacheva, E. Rabinovich, V. Privalov, S. Povolotskaya, V. Shorokhova, S. Sokolova, V. Turdakova, E. Ryzhova, P. Hall, A. B. Schneider, D. L. Preston, E. Ron, *Radiat. Res.* **2006**, *166*, 715.
- [3] D. M. Taylor, *J. Radioanal. Chem.* **1981**, *65*, 195.
- [4] B. J. Riley, J. D. Vienna, D. M. Strachan, J. S. McCloy, J. L. Jerden, *J. Nucl. Mater.* **2016**, *470*, 307.
- [5] S. U. Nandanwar, K. Coldsnow, V. Utgikar, P. Sabharwall, D. Eric Aston, *Chem. Eng. J.* **2016**, *306*, 369.
- [6] W. Xie, D. Cui, S.-R. Zhang, Y.-H. Xu, D.-L. Jiang, *Mater. Horiz.* **2019**, *6*, 1571.
- [7] Y.-N. Yu, Z. Yin, L.-H. Cao, Y.-M. Ma, *J. Incl. Phenom. Macrocycl. Chem.* **2022**, *102*, 395.
- [8] A. I. Cooper, *ACS Cent. Sci.* **2017**, *3*, 544.
- [9] M. A. Little, A. I. Cooper, *Adv. Funct. Mater.* **2020**, *30*, 1909842.
- [10] T.-H. Niu, C.-C. Feng, C. Yao, W.-Y. Yang, Y.-H. Xu, *ACS Appl. Polym. Mater.* **2021**, *3*, 354.
- [11] P. Wang, Q. Xu, Z. Li, W. Jiang, Q. Jiang, D. Jiang, *Adv. Mater.* **2018**, *30*, 1801991.
- [12] X. Jiang, X. Cui, A. J. E. Duncan, L. Li, R. P. Hughes, R. J. Staples, E. V. Alexandrov, D. M. Proserpio, Y. Wu, C. Ke, *J. Am. Chem. Soc.* **2019**, *141*, 10915.
- [13] L. Xie, Z. Zheng, Q. Lin, H. Zhou, X. Ji, J. L. Sessler, H. Wang, *Angew. Chem.* **2022**, *61*, 202113724.
- [14] D. Dai, J. Yang, Y.-C. Zou, J.-R. Wu, L.-L. Tan, Y. Wang, B. Li, T. Lu, B. Wang, Y.-W. Yang, *Angew. Chem., Int. Ed.* **2021**, *60*, 8967.
- [15] C. Liu, W. Li, Y. Liu, H. Wang, B. Yu, Z. Bao, J. Jiang, *Chem. Eng. J.* **2022**, *428*, 131129.
- [16] C. Liu, Y. Jin, Z. Yu, L. Gong, H. Wang, B. Yu, W. Zhang, J. Jiang, *J. Am. Chem. Soc.* **2022**, *144*, 12390.
- [17] J.-R. Wu, Y.-W. Yang, *Angew. Chem., Int. Ed.* **2021**, *60*, 1690.
- [18] Z. Yan, Y. Yuan, Y. Tian, D. Zhang, G. Zhu, *Angew. Chem.* **2015**, *127*, 12924.
- [19] Y. Zhu, Y.-J. Ji, D.-G. Wang, Y. Zhang, H. Tang, X.-R. Jia, M. Song, G. Yu, G.-C. Kuang, *J. Mater. Chem. A* **2017**, *5*, 6622.
- [20] Y. Chen, H. Sun, R. Yang, T. Wang, C. Pei, Z. Xiang, Z. Zhu, W. Liang, An Li, W. Deng, *J. Mater. Chem. A* **2015**, *3*, 87.
- [21] C. Wang, Y. Wang, R. Ge, X. Song, X. Xing, Q. Jiang, H. Lu, C. Hao, X. Guo, Y. Gao, D. Jiang, *Chemistry* **2018**, *24*, 585.
- [22] J. Jiao, W. Xie, Y. Li, C. Lin, J. Jiang, L. Wang, *Chemistry* **2022**, *28*, 202201933.
- [23] X. Zhang, J. Maddock, T. M. Nenoff, M. A. Denecke, S. Yang, M. Schröder, *Chem. Soc. Rev.* **2022**, *51*, 3243.
- [24] Y. Liao, J. Weber, B. M. Mills, Z. Ren, C. F. J. Faul, *Macromolecules* **2016**, *49*, 6322.
- [25] X. Qian, B. Wang, Z.-Q. Zhu, H.-X. Sun, F. Ren, P. Mu, C. Ma, W.-D. Liang, A. Li, *J. Hazard. Mater.* **2017**, *338*, 224.
- [26] Y. Xie, T. Pan, Q. Lei, C. Chen, X. Dong, Y. Yuan, J. Shen, Y. Cai, C. Zhou, I. Pinnau, Y. Han, *Angew. Chem.* **2021**, *133*, 22606.
- [27] M. Zhang, Y. Li, W. Yuan, X. Guo, C. Bai, Y. Zou, H. Long, Y. Qi, S. Li, G. Tao, C. Xia, L. Ma, *Angew. Chem., Int. Ed.* **2021**, *60*, 12396.
- [28] X. Qian, Z.-Q. Zhu, H.-X. Sun, F. Ren, P. Mu, W. Liang, L. Chen, A. Li, *ACS Appl. Mater. Interfaces* **2016**, *8*, 21063.
- [29] F. Ren, Z. Zhu, X. Qian, W. Liang, P. Mu, H. Sun, J. Liu, A. Li, *Chem. Commun.* **2016**, *52*, 9797.
- [30] K. Jie, Y. Zhou, E. Li, F. Huang, *Acc. Chem. Res.* **2018**, *51*, 2064.
- [31] G. R. Desiraju, *J. Am. Chem. Soc.* **2013**, *135*, 9952.
- [32] H.-W. Schmidt, F. Würthner, *Angew. Chem., Int. Ed.* **2020**, *59*, 8766.
- [33] C. Kulkarni, E. W. Meijer, A. R. A. Palmans, *Acc. Chem. Res.* **2017**, *50*, 1928.
- [34] Y. Zhong, Y. Yang, Y. Shen, W. Xu, Q. Wang, A. L. Connor, X. Zhou, L. He, X. C. Zeng, Z. Shao, Z.-L. Lu, B. Gong, *J. Am. Chem. Soc.* **2017**, *139*, 15950.
- [35] T. Marmin, Y. L. Dory, *Chemistry* **2019**, *25*, 6707.
- [36] N. Nazari, S. Bernard, D. Fortin, T. Marmin, L. Gendron, Y. L. Dory, *Chemistry* **2023**, *29*, 202203717.
- [37] Z. Dai, L. Liu, Z. Zhang, *Adv. Mater.* **2019**, *31*, 1805417.
- [38] L. Chen, B. Zhang, L. Chen, H. Liu, Y. Hu, S. Qiao, *Mater. Adv.* **2022**, *3*, 3680.
- [39] J. Yang, J. Wang, B. Hou, X. Huang, T. Wang, Y. Bao, H. Hao, *Chem. Eng. J.* **2020**, *399*, 125873.
- [40] B. Wang, R.-B. Lin, Z. Zhang, S. Xiang, B. Chen, *J. Am. Chem. Soc.* **2020**, *142*, 14399.
- [41] S. Nandi, D. Chakraborty, R. Vaidyanathan, *Chem. Commun.* **2016**, *52*, 7249.
- [42] B. Wang, R. He, L.-H. Xie, Z.-J. Lin, X. Zhang, J. Wang, H. Huang, Z. Zhang, K. S. Schanze, J. Zhang, S. Xiang, B. Chen, *J. Am. Chem. Soc.* **2020**, *142*, 12478.
- [43] Q. Yin, P. Zhao, R.-J. Sa, G.-C. Chen, J. Lü, T.-F. Liu, R. Cao, *Angew. Chem., Int. Ed.* **2018**, *57*, 7691.
- [44] Z. Ke, K. Chen, Z. Li, J. Huang, Z. Yao, W. Dai, X. Wang, C. Liu, S. Xiang, Z. Zhang, *Chin. Chem. Lett.* **2021**, *32*, 3109.
- [45] P. Li, M. R. Ryder, J. F. Stoddart, *Acc. Mater. Res.* **2020**, *1*, 77.
- [46] N. Malek, T. Maris, M. Simard, J. D. Wuest, *J. Am. Chem. Soc.* **2005**, *127*, 5910.
- [47] K. E. Maly, E. Gagnon, T. Maris, J. D. Wuest, *J. Am. Chem. Soc.* **2007**, *129*, 4306.
- [48] P. Li, Y. He, J. Guang, L. Weng, J. C.-G. Zhao, S. Xiang, B. Chen, *J. Am. Chem. Soc.* **2014**, *136*, 547.
- [49] X. Song, Y. Wang, C. Wang, D. Wang, G. Zhuang, K. O. Kirlikovali, P. Li, O. K. Farha, *J. Am. Chem. Soc.* **2022**, *144*, 10663.
- [50] Z. Zhang, Y. Ye, S. Xiang, B. Chen, *Acc. Chem. Res.* **2022**, *55*, 3752.
- [51] R.-B. Lin, B. Chen, *Chem* **2022**, *8*, 2114.
- [52] P. Baillargeon, Y. L. Dory, *Cryst. Growth Des.* **2009**, *9*, 3638.
- [53] N. Kobko, L. Paraskevass, E. Del Rio, J. J. Dannenberg, *J. Am. Chem. Soc.* **2001**, *123*, 4348.
- [54] N. Kobko, J. J. Dannenberg, *J. Phys. Chem. A* **2003**, *107*, 10389.
- [55] A. S. Mahadevi, G. N. Sastry, *Chem. Rev.* **2016**, *116*, 2775.
- [56] X.-Z. Luo, X.-J. Jia, J.-H. Deng, J.-L. Zhong, H.-J. Liu, K.-J. Wang, D.-C. Zhong, *J. Am. Chem. Soc.* **2013**, *135*, 11684.
- [57] S. B. Alahakoon, K. Tan, H. Pandey, S. D. Diwakara, G. T. Mccandless, D. I. Grinffiel, A. Durand-Silva, T. Thonhauser, R. A. Smaldone, *J. Am. Chem. Soc.* **2020**, *142*, 12987.
- [58] J. D. Wuest, *Chem. Commun.* **2005**, *47*, 5830.
- [59] S. Kumar, S. Bera, S. K. Nandi, D. Haldar, *Soft Matter* **2021**, *17*, 113.
- [60] C. Zehe, M. Schmidt, R. Siegel, K. Kreger, V. Daebel, S. Ganzleben, H.-W. Schmidt, J. Senker, *CrystEngComm* **2014**, *16*, 9273.
- [61] J. M. Word, S. C. Lovell, J. S. Richardson, D. C. Richardson, *J. Mol. Biol.* **1999**, *285*, 1735.
- [62] M. Suzuki, J. F. K. Kotyk, S. I. Khan, Y. Rubin, *J. Am. Chem. Soc.* **2016**, *138*, 5939.
- [63] J. J. Van Gorp, J. A. J. M. Vekemans, E. W. Meijer, *J. Am. Chem. Soc.* **2002**, *124*, 14759.
- [64] C. Zhao, Q.-F. Sun, W. M. Hart-Cooper, A. G. Dipasquale, F. D. Toste, R. G. Bergman, K. N. Raymond, *J. Am. Chem. Soc.* **2013**, *135*, 18802.
- [65] K. Uemura, S. Kitagawa, K. Fukui, K. Saito, *J. Am. Chem. Soc.* **2004**, *126*, 3817.
- [66] S. Cantekin, T. F. A. De Greef, A. R. A. Palmans, *Chem. Soc. Rev.* **2012**, *41*, 6125.

- [67] M. Iyoda, S. Sirinintasak, Y. Nishiyama, A. Vorasingha, F. Sultana, K. Nakao, Y. Kuwatani, H. Matsuyama, M. Yoshida, Y. Miyake, *Synthesis* **2004**, *09*, 1527.
- [68] M. Kiguchi, K. Tahara, Y. Takahashi, K. Hasui, Y. Tobe, *Chem. Lett.* **2010**, *39*, 788.
- [69] C. A. Jiménez, J. B. Belmar, L. Ortíz, P. Hidalgo, O. Fabelo, J. Pasán, C. Ruiz-Pérez, *Cryst. Growth Des.* **2009**, *9*, 4987.
- [70] V. Nagarajan, V. R. Pedireddi, *Cryst. Growth Des.* **2014**, *14*, 1895.
- [71] S. Torquato, F. H. Stillinger, *Rev. Mod. Phys.* **2010**, *82*, 2633.
- [72] Y. S. Ho, G. Mckay, *Process Biochem.* **1999**, *34*, 451.
- [73] X. Guo, Y. Li, M. Zhang, K. Cao, Y. Tian, Y. Qi, S. Li, K. Li, X. Yu, L. Ma, *Angew. Chem., Int. Ed.* **2020**, *59*, 22697.
- [74] A. Sen, S. Sharma, S. Dutta, M. M. Shirodkar, G. K. Dam, S. Let, S. K. Ghosh, *ACS Appl. Mater. Interfaces* **2021**, *13*, 34188.
- [75] P. Petrache, S. Rodino, M. Butu, G. Pribac, M. Pentea, M. Butnariu, *Dig. J. Nanomater. Biostructures* **2014**, *9*, 1523.
- [76] S. L. Hsu, A. J. Signorelli, G. P. Pez, R. H. Baughman, *J. Chem. Phys.* **1978**, *69*, 106.
- [77] J. Cambedouzou, J.-L. Sauvajol, A. Rahmani, E. Flahaut, A. Peigney, C. Laurent, *Phys. Rev. B* **2004**, *69*, 235422.
- [78] L. Yang, S. S. Saavedra, N. R. Armstrong, *Anal. Chem.* **1996**, *68*, 1834.
- [79] A. Maliakal, L. Reith, S. Cabot, *Appl. Phys. Lett.* **2016**, *108*, 153109.
- [80] L. J. Barbour, *Chem. Commun.* **2006**, *11*, 1163.